Lab on a Chip

Accepted Manuscript

RSC Publishing

www.rsc.org/loc
Registered Charity Number 207890

A neutral droplet splits into two oppositely charged daughter droplets at a T-junction in presence of an electric field. The droplet net charge can be precisely tuned by the charging voltage for droplet control and manipulation.

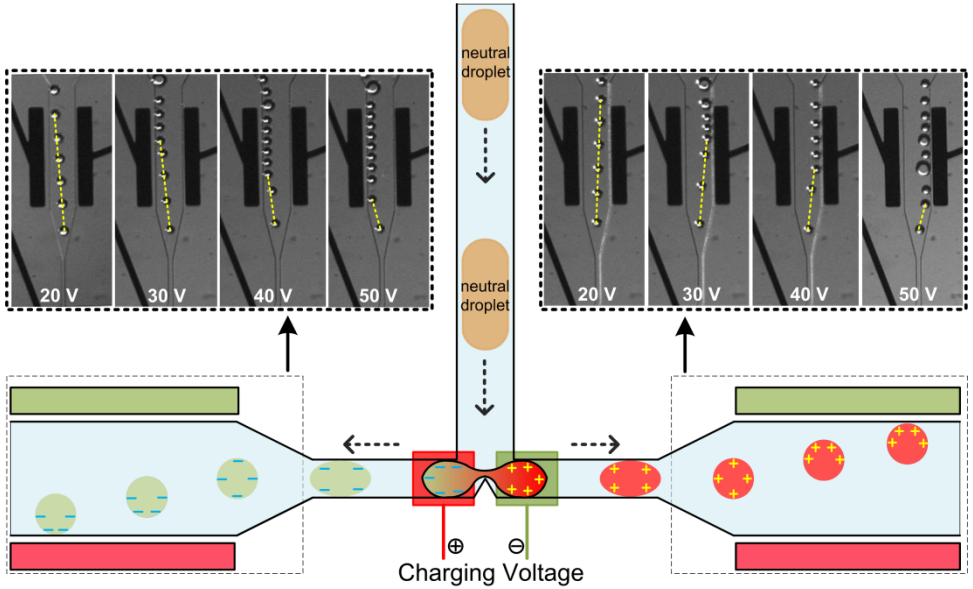

Cite this: DOI: 10.1039/c0xx00000x

www.rsc.org/xxxxxx

ARTICLE TYPE

Electrostatic charging and control of droplets in microfluidic devices

Hongbo Zhou[a,b] and Shuhuai Yao*[a]

Received (in XXX, XXX) Xth XXXXXXXXX 20XX, Accepted Xth XXXXXXXXX 20XX
DOI: 10.1039/b000000x

Precharged droplets can facilitate manipulation and control of low-volume liquids in droplet-based microfluidics. In this paper, we demonstrate non-contact electrostatic charging of droplets by polarizing a neutral droplet and splitting it into two oppositely charged daughter droplets in a T-junction microchannel. We performed numerical simulation to analyze the non-contact charging process and proposed a new design with a notch at the T-junction in aid of droplet splitting for more efficient charging. We experimentally characterized the induced charge in droplets in microfabricated devices. The experimental results agreed well with the simulation. Finally, we demonstrated highly effective droplet manipulation in a path selection unit appending to the droplet charging. We expect our work could enable precision manipulation of droplets for more complex liquid handling in microfluidics and promote electric-force based manipulation in 'lab-on-a-chip' systems.

Introduction

Droplets in microfluidic systems can work as 'miniaturized laboratories'[1] for their unique features such as high-throughput, minimal reagent consumption, contamination-free, fast response, and isolation of individual space[2, 3], and therefore droplet-based microfluidics has recently emerged as a potential platform for chemical and biological assays[4, 5], synthesis[6], reactions[7], and high throughput screening[5, 8]. In these applications, the basic droplet manipulation techniques including forming[9,10], transporting[11], merging[12,13], splitting[14], sorting[10] and storing[15]) have been developed with the aid of acoustic wave[16], surface tension[8,13], electric[10], magnetic[17], thermal[18,19], optical[20,21], and hydrodynamic forces[13, 22], etc.

Among these manipulation schemes, electric force is one of the most promising methods, not only for its shorter response time, but also for its good compatibility and integratiblity with microfluidic systems. According to electrodynamics theory, the electric force acting on a dielectric particle can be expressed as, $\vec{F} = q\vec{E} + (\vec{p}\cdot\nabla)\vec{E}$, where q is the free charge of the particle, $\vec{E}$ is the electric field, and $\vec{p}$ represents the dipole moment induced by the external field. The second term in this formula refers to the dielectrophoretic (DEP) force, based on which droplets sorter[23,24], trapping[25] and releasing[15] have been demonstrated successfully. However, due to its dependence on the gradient of electric field, a high voltage (usually greater than 1 kV) is needed to produce sufficient forces in these applications. Another phenomenon, electrowetting, has also been utilized in various digital microfluidic devices[11,26-28]. In these devices, highly integrated electrodes and precise controlling strategy are essential to form non-uniform electric fields to regulate the surface wetting properties and control droplets' moving direction. Whereas the first term (i.e., electrostatic force) is adopted for charged particles, electrostatic force can act on them directly and scales with the amount of net charges, both of which can efficiently lower the controlling voltage and facilitate droplet manipulation with better controllability[29]. Charging droplets by contact-release method has been demonstrated by several groups[29-35]. In their work, droplets firstly contact with bare electrodes, then obtain charges in electric fields, and finally keep a certain amount of net charges after being released. However, sample contamination and electrochemical reactions may take place at the electrode/droplet interface[32,33] without any shield. To eliminate these problems, a novel non-contact charging method was proposed by Link et al.[36], in which a bifurcation microchannel was used to split a neutral droplet into two daughter droplets. In the presence of an electric field, the neutral droplet was polarized prior to separation, resulting in two oppositely charged daughter droplets. However, their simple design has not been carefully analyzed and characterized. The working principle and charge quantification of the system remains elusive for precise control of droplets in practical systems.

To realize this non-contact charging method, we performed both numerical and experimental studies for charging droplets in a T-junction microchannel with embedded electrodes. Using numerical methods for two-phase flow coupling with electrostatics, for the first time, the mechanism of charging process was simulated and analyzed. A new design for more efficient charging was proposed based on the simulation results. Microfluidic devices of the proposed design were developed using standard microfabrication technology. The induced charge in a droplet was characterized by measuring the droplet trajectory in presence of a transverse electric field. Finally, as a proof of concept, a path selection unit appending to the droplet charging was developed and highly effective droplet manipulation was demonstrated using a controlling voltage of 60 V.

Methods and materials

A. Working mechanism

The principle of the droplet charging process in a T-junction microchannel is illustrated in Fig.1. A neutral water droplet travels along the vertical channel and is entering the T-junction bifurcation where a pair of charging electrodes are embedded symmetrically and covered by a dielectric layer. When a positive or negative pulse is applied to the charging electrodes, opposite charges is induced on the water-oil interface. The induced charges are trapped and distributed on the surface of the droplet. The amount and polarity of the charges can be controlled by the voltage applying on the charging electrodes (Fig. 1a). Then the droplet is stretched by hydrodynamic force[14] at the T-junction, a cylindrical liquid thread is formed and connects two rears of the droplet at both sides (Fig. 1b). As the stretching process continues, the circumference of the thread becomes thinner gradually, which triggers the onset of the Rayleigh-Plateau (R-P) instability[14,37]. In consequence, the liquid thread breaks up, and the induced charges remain in the two separated new droplets (Fig. 1c). In this way, two daughter droplets with opposite net charges are obtained. The total capacitance of the induction electrodes, dielectric layer and the droplet constitute capacitors in series can be estimated as (shown in Fig. 1a), $C_{whole}=C_{interface}$ || C_{drop} || $C_{interface}$, where $C_{interface}$ represents the capacitor formed by the electrode-dielectric layer-droplet interface. And the total capacitance varies as droplet reshapes in the stretching and splitting process. If $V_{charging}$ is applied across the induction electrodes, the induced charge would be $Q = C_{whole}*V_{charging}$ in the A' part and B' part of the droplet.

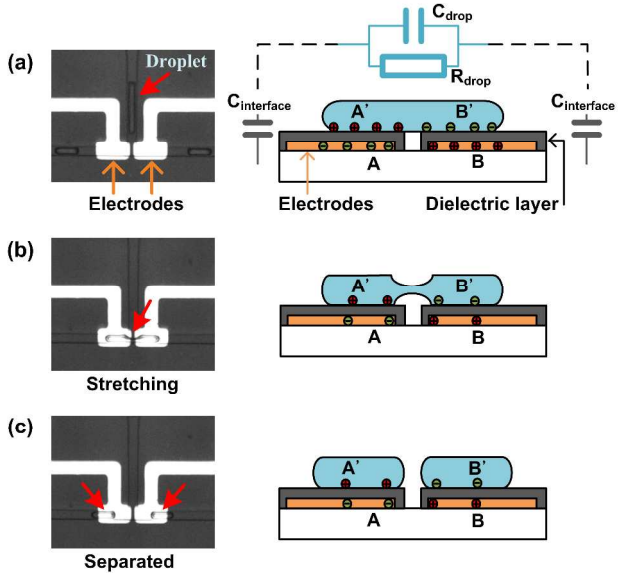

Fig.1 Principle of the charging process. The left column is the top view and the right column is the side view. (a) a neutral droplet travels to the induction electrodes and, charges are induced and distributed on the surface. (b) a droplet is stretched at the T-junction by hydrodynamic force. (c) a droplet is divided into two daughter droplets with opposite net charges.

The time scale of the stretching and splitting process is estimated to be several milliseconds, whereas the charge relaxation time for the ions to respond to the induction electric field can be calculated as[29]: $\tau = \varepsilon/\sigma = 0.125$ ms, where ε and σ are permittivity and electrical conductivity of water, respectively. The charge relaxation time is one order shorter than that of the droplet reshaping and splitting process. Therefore, the ultimate charge in droplet A' and B' (Fig. 1c) is determined by the capacitance of the whole system at the instant of droplet separation ($C_{separation}$), $Q = V_{charging}*C_{separation}$. It should be mentioned that, in theory, the maximum throughput of the charging procedure is limited by the charge relaxation time. For pure water, the charge relaxation time is so short (0.125 ms) that the droplet charging frequency can be achieved at several thousands per second, which meets the requirement for high thoughput applications.

B. Numerical simulation

In order to quantify the amount of induced charge in droplets, we performed numerical situations to capture the droplet dynamics and variation of the system capacitance during the droplet splitting and reshaping. The simulation was conducted using a commercial finite element code, COMSOL 3.5a (Comsol, Inc.), based on the laminar two-phase flow level-set module coupling with the electrostatic module. Forces other than electrostatic forces (e.g., dielectrophoretic, electrowetting electrophoresis, etc) were neglected in our simulation for relatively low electric field (~10^5 V/m).

First, the interface between the immiscible water and oil phases is tracked using the level set method[38], in which the interface is represented by the level set function ϕ[39]. The velocity field of two-phase flow in the simulation is governed by the incompressible Navier-Stokes equations:

$$\frac{\partial \rho}{\partial t} + \nabla \cdot (\rho \vec{u}) = 0 \tag{1}$$

$$\rho \frac{\partial \vec{u}}{\partial t} + \rho(\vec{u} \cdot \nabla)\vec{u} = -\nabla p + \nabla \cdot (\mu \nabla \vec{u}) + \vec{F}_{st} \tag{2}$$

$$\rho = \rho_1 + (\rho_2 - \rho_1)\phi\,,\ \mu = \mu_1 + (\mu_2 - \mu_1)\phi \tag{3}$$

where ρ_1 and ρ_2 are the fluid densities of dispersed phase and continuous phase, u is the flow velocity, t represents the time, p is the pressure, μ_1 and μ_2 denote the dynamic viscosities of dispersed phase and continuous phase. The body force $\vec{F}_{st}$ is caused by the surface tension, $\vec{F}_{st} = \sigma\kappa\delta\vec{n}$, where σ is the interfacial tension between two phases, κ is the curvature, δ is a Dirac delta function concentrated to the interface, and $\vec{n}$ is the unit normal to the interface. The motion of the water-oil interface is tracked by solving the equation for ϕ:

$$\frac{\partial \phi}{\partial t} + u \cdot \nabla \phi = \gamma \nabla \cdot (\varepsilon \nabla \phi - \phi(1-\phi)\frac{\nabla \phi}{|\nabla \phi|}) \tag{4}$$

where γ determines the amount of reinitialization of the level set function and ε determines the thickness of the interface. $\gamma = 0.1$ and $\varepsilon = 0.8E\text{-}6$ are used in our specific simulations.

Second, the electric field in the droplet, oil and dielectric layers is calculated by the Poisson equation:

$$\nabla \cdot (\varepsilon_o \varepsilon_r \nabla \varphi) = \rho_f \tag{5}$$

where φ is the electric potential, ρ_f denotes the free net charge density, $\varepsilon_0\varepsilon_r$ represents the permittivity of the related medium in the field. The Poisson equation is coupled with the two-phase flow equations through the distribution of different dielectric materials (water, oil, PDMS, and silicon oxide), and the electric field (E) is instantaneously calculated during the droplet splitting and reshaping process. The system capacitance is calculated in the electrostatic module by:

$$C = \frac{2U_e}{V^2} \tag{6}$$

$$U_e = \frac{1}{2}\varepsilon_0\varepsilon_r \int_\Omega |E|^2 d\Omega \tag{7}$$

where V is the potential difference between the two induction electrodes, U_e and E are the electrical energy stored and the electric field in the domain, respectively. Ω denotes the entire computational domain in the model.

C. Device fabrication and instruments

The device consists of a poly(dimethylsiloxane) (PDMS) layer containing microfluidic channels and an electrode-patterned quartz substrate. The microchannels were fabricated in PDMS using a standard soft lithography procedure. A negative photoresist (SU-8 2050, MicroChem) was spin-coated and patterned on a silicon wafer. The developed SU-8 pattern yielded a mold for microchannels of 50 μm deep. The mold was then placed in a desiccator with a few drops of trichloro(1H,1H,2H,2H-perfluorooctyl)silane (Sigma-Aldrich) to aid removal of the PDMS layer from the mold. PDMS mixture in a 10:1 ratio of prepolymer and curing agent (Sylgard 184, Dow Corning) was degassed and poured over the mold and cured in an 80 °C oven for an hour. The cast PDMS was then peeled off from the mold and inlet and outlet holes were punched using a pan head needle on the PDMS replica. To make the microelectrodes, an adhesive layer of Ti/W (200 Å) and 1500 Å of platinum were sputtered on a photoresist patterned quartz wafer, and a lift-off process was applied to form the electrode patterns. Then an insulation layer of silicon oxide with a thickness of 1 μm was deposited on the patterned quartz substrate using PECVD, and finally the contacting pads for electrical connection were exposed. The PDMS replica and quartz substrate were cleaned, treated with oxygen plasma, aligned under the microscope and then bonded together to seal the microchannels. The bonded device was heated at 105 °C on a hotplate for 24 h to increase bonding strength and recover the hydrophobicity of PDMS-based microchannels.

Syringe pumps (KD Scientific) were used to deliver the mineral oil and DI water into the microchannels at a range of flow rates. An inverted microscope (Eclipse Ti, Nikon) with a CCD camera (EXi Blue, Q-IMAGING) was used to to capture the droplets moving in the microchannels. Two source meters (Keithley 2400) were used to supply DC voltages to the induction and controlling electrodes and monitor the currents spontaneously.

Results and discussion

A. Simulation results

The dynamic process of droplet splitting and charging was simulated for two designs: a T-shaped microchannel (Fig. 2a) and a modified design with a triangle notch at the T-junction (Fig.2b).

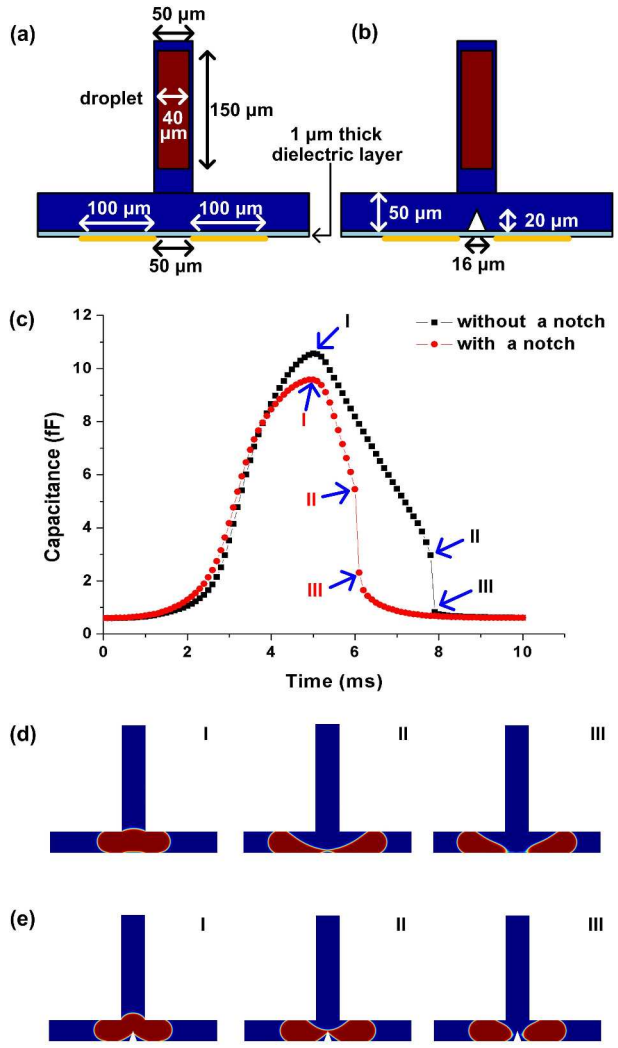

Fig. 2 Simulation of the charging process. (a) and (b) 2D computational domain for the T-channels without and with a notch, respectively. (c) The capacitance of the whole system during the splitting process. (d) and (e) Snap images of the droplets at the critical instants (indicated in Fig. 2c) during the splitting process in the T- channels without and with a notch, respectively.

The droplet was initially set in rectangular shape (6000 μm^2, estimated from the captured CCD images in experiments) with two parallel aqueous phases in the continuous oil phase. Two electrodes with a length of 100 μm were set symmetrically across the T-junction as indicated. The SiO_2 dielectric layer was modeled as a 1 μm thick line between the electrodes and microchannel walls. The inlet velocity of the continuous phases was set as 28.7 mm/s, in order to match the droplet velocity in the experiments. The physical parameters used in the simulation are summarized in Table 1.

Table 1 Physical properties[38]

Density of water, ρ1	1008 kg/m^3
Density of mineral oil, ρ2	840 kg/m^3
Dynamic viscosity of water, μ1	1.02 mPa•s
Dynamic viscosity of mineral oil, μ2	30 mPa•s
Interfacial tension, σ	38 mN/m
Relative dielectric constant of water	78
Relative dielectric constant of PDMS	2.8
Relative dielectric constant of mineral oil	2.5
Relative dielectric constant of silicon oxide	3.9

The simulation results of the two designs are shown in Fig. 2c-e. The system capacitance is calculated from Eqs. (6) and (7), and its value varies as one droplet travels from the center channel to the T-junction, stretches and splits into two droplets. As shown in Fig. 2c, three critical points (I, II, III) in the time-dependent capacitance curves indicate the corresponding steps (I, II, III) that are depicted in Fig. 2d and e for the two designs, respectively. The system capacitance increases firstly as the droplet moves into the T-junction, and reaches the maximum at point I. This is reasonable, since the permittivity of droplet (water) is much higher than that of the surrounding mineral oil. When the droplet moves closer to the T-junction, more space between two electrodes is filled by water instead of oil. When the space is filled with water (Fig. 2d-I and 2e-I), the system capacitance reaches the maximum. After this moment, the droplet stretches and part of spaces is replaced by oil, which causes the capacitance to drop again. The stretching process and capacitance falling-down trend continue until the R-P instability (when the tinning thread of the droplet starts to break) takes place. Fig.2d-II and 2e-II indicate the instant just before the separation. Then, the liquid thread breaks rapidly (Fig. 2d-III and 2e-III), leading to a sudden drop of the capacitance (as shown in Fig. 2c from point II to point III). Our simulation results are consistent with the work of capacitive sensing of droplets by Elbuken et al.[40], in which they demonstrated that the capacitance firstly increased and then decreased when the droplet entered and left the sensing electrodes, and saturated once the entire droplet was in the sensing region.

As mentioned above, the ultimate net charge in daughter droplets are determined by the capacitance at the instant of separation. However, in the original T-junction, a long and slim liquid thread (Fig.2d-II) would reduce the total capacitance severely (from 10.71 fF to 2.98 fF in our simulation). In order to alleviate this reduction, an isosceles triangle (with a height of 20 μm and a base of 16 μm) shaped notch is symmetrically set at the T-junction to accelerate the R-P instability and speed up the splitting process[37]. The red curve in Fig.2c is the time-dependent capacitance curve for this new design. At the instant of separation, the system capacitance is increased from 2.98 fF to 5.47 fF compared to the original design. As shown in Fig. 2d-II and 2e-II, the break-up of the liquid thread is facilitated by the triangle notch without much stretching and elongation.

We also performed numerical simulations to study the droplet size effect and found that the size of the droplet can affect the whole system capacitance (details could be found in the Electronic Supplementary Information). When the droplet is small and partially covers the charging electrodes at the separating instant at the T-junction, the whole system capacitance is relatively lower. When the droplet size increases and fully covers the charging electrodes (the projected area of the droplet is > 6000 μm^2), the whole system capacitance eventually would approaches a constant value. For a droplet of specific size, the system capacitance and corresponding induced charges can be obtained from the simulation model.

It should be mentioned that use of surfactant may help the system stabalization[41]. However, due to the low water-oil interfacial tension, this would cause a longer and slimmer liquid thread before the separation instant and subsequently decrease the system capacitance (details could be found in the Electronic Supplementary Information). In order to obtain higher charging efficiency, surfactants should be avoided during the charging process.

B. Experimental results

Characterization of induced charge in droplets

We also experimentally measured the amount of induced charges in droplets for the two designs. In the characterization device, droplets are firstly formed using a flow focusing structure, travel to the T-junction where the droplets are charged and split. Then, these precharged droplets flow into the testing channels for charge quantifitation. As shown in Fig. 3, two testing channels (with a width of 200 μm) and two pairs of deflecting electrodes (with an interval of 240 μm) were added symmetrically on both sides of the T-channel to ensure balanced flow in the device. Droplet displacement was measured in the testing channel in presence of a transverse electric field (E_d).

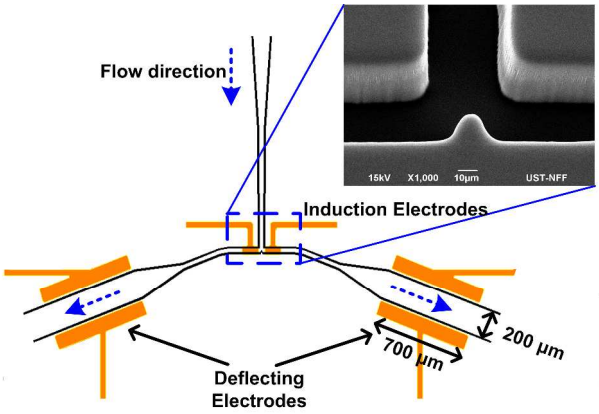

Fig. 3 Schematic illustration of the device for measuring the induced charge in a droplet. The inset is an SEM image of the T-junction with a notch at the center.

The charge quantification is based on a hydrodynamic model of droplet trajectory[31,42]. In the testing channel, a charged droplet is driven by the electrostatic force (F_E) and viscous drag force (F_D):

$$m\frac{d^2y}{dt^2} = F_E + F_D = qE_d - 6\pi r\eta\frac{dy}{dt} \qquad (8)$$

where y is the displacement of the droplet perpendicular to the flow direction, q is the net charge in the droplet, E_d is the transverse electric field applied across the defecting electrodes, m is the mass of the droplet, r is the radius of a spherical droplet, η is the dynamic viscosity of the oil phase, and t is the time of the

droplet traveling along the testing channel. The solution to Eq. (8) is given as[31,42].

$$y = \frac{qE_d}{6\pi r\eta}t + \frac{qE_d r}{27\pi\eta^2}(e^{-\frac{9\eta\cdot t}{2r^2\rho}} - 1) \quad (9)$$

The exponential term in Eq. (9) is negligible due to the small size of our droplets (e.g., the equivalent radius of the droplet r = 30 μm and the time for the droplet travelling through the testing channel t > 60 ms): $t/r >> 2\rho r/9\eta$, where ρ is the density of the droplet. So that, the droplet charge can be approximated as

$$q = \frac{6\pi\cdot r\eta}{E_d}\cdot\frac{y}{t} \quad (10)$$

Thus, for a given deflecting voltage, the droplet charge can be obtained by measuring the droplet displacement as a function of the travelling time. In our experiments, a constant voltage of 20 V was applied to the defecting electrodes, and the transverse electric field is estimated to be 83 kV/m. The droplet charge was tuned by the charging voltage (stepping from -50V to 50 V). The displacement of charged droplets in the testing channel was recorded by a CCD camera (as shown in Fig. 4).

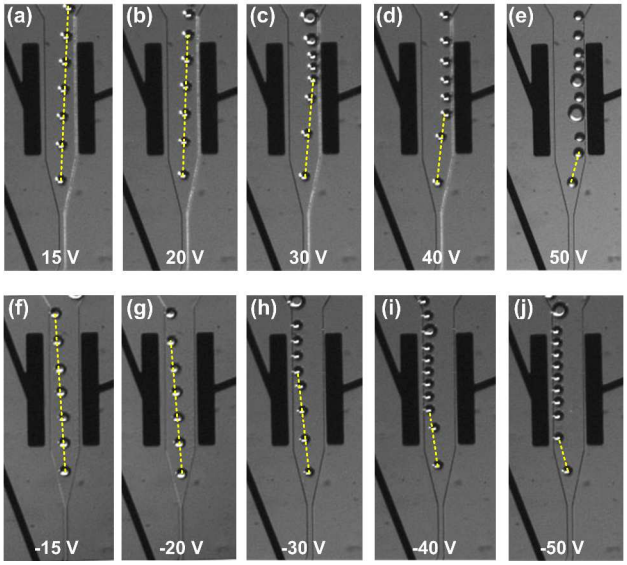

Fig. 4 Deflection of droplets with different amount of charge under a constant deflecting voltage of 20 V. The charging voltage was 15 V for (a), 20 V for (b), 30 V for (c), 40 V for (d), 50 V for (e), -15 V for (f), -20 V for (g), -30 V for (h), -40 V for (i) and -50 V for (j). The equivalent diameter of the precharged droplets was ~60 μm. Some larger droplets were formed near the channel walls (e.g., in Fig. 4e) due to the merging of two adjacent droplets at low velocity near the walls. The yellow dotted line indicates the trajectory of the droplets in the testing channel.

In Fig. 4 a-e, the droplets show increasing displacement in the transverse direction as the charging voltage increase from 15 to 50 V. For nagative charging voltages (from -15 to -50 V in Fig. 4 f-j), the direction of droplet displacement became opposite and the magnitude changed accordingly. The displacement (y) and the traveling time (t) were directly measured from the CCD images. Then, the amount of induced charge was calculated from Eq. (10) and the value versus the charging voltage (symbols) is plotted in Fig. 5. Solid lines are the simulation results for the fabricated devices of the two designs.

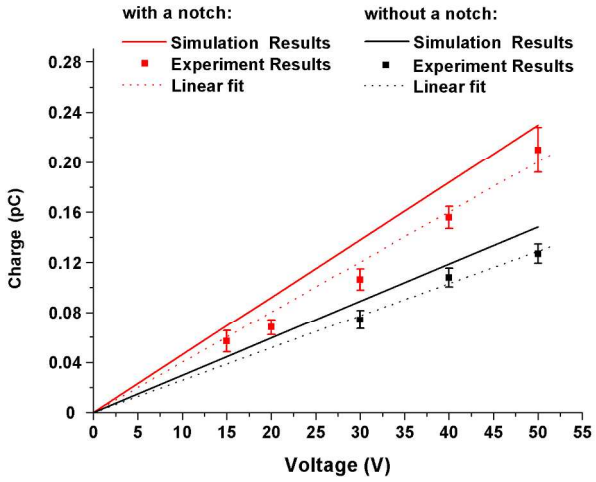

Fig. 5 Induction charge versus charging voltage. The data in the third quadrant (negative charge and voltage) were omitted since they were almost symmetric to the data in the first quadrant.

The slope of the charge-voltage curve represents the system capacitance. The linear fits of the experimental data (dotted lines) yield 4.12 fF and 2.60 fF for the designs with and without a notch, respectively, while 4.61 fF and 2.98 fF were obtained in the simulations. It should be noted that the fabricated notch (inset of Fig. 3) has a round tip instead of a sharp one, reducing the capacitance from 5.47 fF (Fig. 2) to 4.61 fF. The relative errors between experimental and simulation results are within 15%. The discrepancy is mainly due to the two-dimensional (2D) model we adopted in the numerical simulations. Although the 2D model can greatly reduce the computation cost, for this practical 3D problem, it may lead to a certain errors. For example, in the 2D model, the thinning liquid thread is treated as a slice normal to the xy-plane, whereas it should be an asymmetrical cylindrical thread in the 3D model. Therefore, the capacitance in the 3D situation should be lower than the 2D simulation results. Nevertheless, our simulation model has revealed the overall trend of the charging process, and therefore may serve as an effective tool for analyzing and optimizing the designs for droplet-based microfluidics.

Due to lack of reported results from the non-contact charging methods, we primarily compare the induced charge in our device with those reported using the direct contact charging methods in droplet-based microfluidics. Ahn et al. reported[31] a direct electrostatic charging method for droplets in microchannels and achieved a charge density per voltage of 2.6E-3 $Cm^{-3}V^{-1}$. While using our non-contact charging, droplet splitting method, we have improved the charge density per voltage by one order of magnitude (2.9E-2 $Cm^{-3}V^{-1}$ in our new design), and moreover, we can obtain positively and negatively charged droplets simultaneously.

Demonstration of a path selection device

In droplet-based microfluidics, droplet selection is an important step to guide droplets in certain direction or to the desired location for further reaction or detection. Here, as a proof of concept, we designed a droplet path selection device based on the precharged droplets. Immediately after the precharging part

(using our new design), a bifurcation was used for directing droplets to the upper and lower branches (with a cross section of 80 × 50 μm^2), as shown in Fig. 6. A pair of selecting electrodes with an interval of 130 μm were located at the entrance of the two branches. In the experiments, the water and total oil flow rates were set as 1 μl/min and 13 μl/min, respectively. By using a flow focusing structure, droplets with a volume of ~0.64 nL were uniformly formed. The resulted droplets after splitting were ~90 μm in diameter, greater than the cross section of the branches, which ensured an additional flow resistance[43] when travelled along the branches.

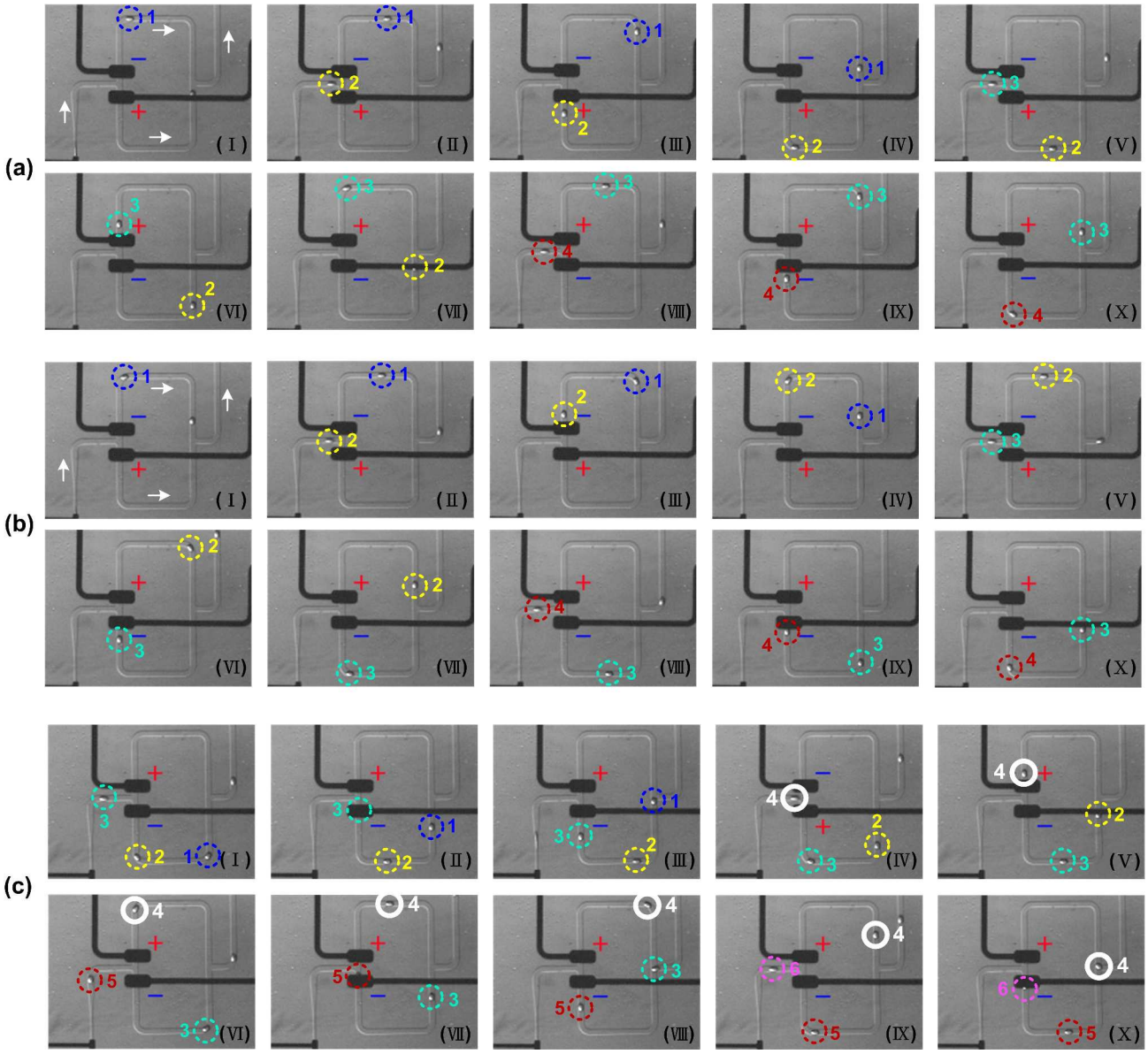

Fig. 6 Snapshots of the path selecting experiments for (a) neutral droplets. (b) and (c) droplets with positive charges. In (a) and (b), a voltage of + / – 60 V (with varied polarity indicated in the images) was applied to the selecting electrodes. In (c), a pulse of – 60 V with duration of 40 ms (in IV) was applied to the selecting electrodes. In the experiments, the droplets were generated at ~ 13 droplets per second.

Fig. 6 shows the experimental results of path selection for neutral and precharged droplets. Droplets were labeled in different numbers (and colors) to denote the droplet moving path (also see Supplementary Movies). Fig. 6a depicts the snapshots of droplets without being charged moving through the upper or lower branches alternately. While the first droplet flowed in the upper branch, an additional flow resistance[43] was added to the upper branch. As a result, the second droplet switched to the lower branch spontaneously. Similarly, when the second droplet stayed in the lower branch and the first droplet had exited the selection path, the third droplet switched to the upper branch again (Fig. 6a(V-VI)). Such one by one selection would continue even if the polarity of the selecting voltage was changed. However, for precharged droplets, the moving path can be intentionally selected by the applied electric fields. Shown in Fig. 6b is one case for directing positively charged droplets by varying the polarity of the selecting voltage. When the selecting electric field was set upwards at the selection entrance, a positively charged droplet (the second droplet in Fig. 6b(II)) moved upwards to the upper branch due to the electrostatic force,

despite that the first droplet had already stayed in the same branch. When the polarity of the selecting voltage was changed, the positively charged droplets were directed into the lower branch (the third and fourth droplets in Fig. 6b(VI-X)). Furthermore, an electric pulse of opposite polarity with duration of 40 ms was applied to the selecting electrodes to select one droplet from a cluster of droplets (Fig. 6c). At the beginning, positively charged droplets moved through the lower branch due to the electrostatic force (Fig. 6c(I)-(III)). When the target droplet (the forth droplet in Fig. 6c(IV)) arrived at the entrance, the electric pulse was applied (by switching the polarity). Thus, the target droplet was selected to the upper branch (Fig. 6c(V)), while the following droplets still moved into lower branches (Fig.6c(VII)-(X)). With the help of an additional detection system (to identify the target droplets) and a trigger system (to precisely apply an electric pulse), this experiment mimics a practical droplet sorter in biological or chemical applications. It should be mentioned that experiments were also performed for negatively charged droplets by switching the polarity of the charging voltage. Similar path selection effect was observed by applying the selecting voltage accordingly.

In the experiments, both charging and selecting voltages were set at 60 V. The system capacitance was 4.63 fF, obtained from the simulation for droplets of 90 μm in diameter. The induced charge in each droplet was estimated to be ~0.25 pC. Under a selecting electric field of 460 kV/m, the net electrostatic force acting on each droplet was calculated as ~0.12 μN at the entrance of the selecting channels. Due to the high charging efficiency of our system, our path selection system has demonstrated 100 % success rate of selection at this low controlling voltage. For practical applications, the lifetime of the charged droplets is another important parameter, which is determined by the electric properties of the surrounding oil. The conductivity of commonly used oil (such as mineral oil or silicone oil) is ~ $1-10\times10^{-12}$ S/m. The charging relaxation time ($\tau = \varepsilon_{oil}/\sigma_{oil}$) is on the order of a few seconds. In the above path selecting experiments, droplets were firstly charged and then transferred to the path selecting unit within 40 ms, which ensured these droplets were sufficiently charged during the selecting procedure. For applications that need charged droplets with longer lifetime, high insulation oil or continuous charging may be adopted.

Conclusion

In summary, we have developed a microfluidic device for non-contact electrostatic charging of droplets. Both simulation and experimental methods were utilized for the characterization of the charging process. According to the simulation and experimental results, for our device, a charging voltage of 10 volt could induce a net charge of ~0.1 pC in a droplet of ~60 μm in diameter, which should be sufficient for droplet manipulation such as fusion, sorting, and trapping. We also demonstrated effective path selection for the precharged droplets in an integrated device. We expect our high-efficiency and contamination-free droplet charging technique can be exploited in other droplet manipulation processes and potentially developed for capacitor-based detection applications.

Acknowledgements

This work was supported by the Direct Allocation Grant (No. DAG12EG07-13) from HKUST and the National Science Foundation of China (No. 61006086). The authors would thank Dr. Liguo Jiang for his useful suggestions.

Notes and references

[a] *Department of Mechanical Engineering, The Hong Kong University of Science and Technology, Hong Kong, China. Tel: 852 2358 7205; E-mail: meshyao@ust.hk*

[b] *Shanghai Institute of Microsystem and Information Technology, Chinese Academy of Science, 865 Changning Road, Shanghai, China.*

† Electronic Supplementary Information (ESI) available: supplementary information about droplet size and surfactant effect on the system capacitance, and the movies of neutral (Moive 1), positively charged droplets (Moive 2) and positively charged droplets under a pulse (Moive 3) moving in the path selction device. See DOI: 10.1039/b000000x/

1. T. A. Franke and A. Wixforth, *ChemPhysChem*, 2008, **9**, 2140-2156.
2. J. Atencia and D. J. Beebe, *Nature*, 2004, **437**, 648-655.
3. H. A. Stone, A. D. Stroock and A. Ajdari, *Annu. Rev. Fluid Mech.*, 2004, **36**, 381-411.
4. J. Pipper, Y. Zhang, P. Neuzil and T. M. Hsieh, *Angewandte Chemie*, 2008, **120**, 3964-3968.
5. B. Zheng, L. S. Roach and R. F. Ismagilov, *Journal of the American Chemical Society*, 2003, **125**, 11170-11171.
6. E. M. Chan, A. P. Alivisatos and R. A. Mathies, *Journal of the American Chemical Society*, 2005, **127**, 13854-13861.
7. D. Belder, *Angewandte Chemie International Edition*, 2005, **44**, 3521-3522.
8. X. Niu, F. Gielen and J. B. Edel, *Nature chemistry*, 2011, **3**, 437-442.
9. S. L. Anna, N. Bontoux and H. A. Stone, *Applied Physics Letters*, 2003, **82**, 364.
10. L. M. Fidalgo, G. Whyte, D. Bratton, C. F. Kaminski, C. Abell and W. T. S. Huck, *Angewandte Chemie International Edition*, 2008, **47**, 2042-2045.
11. S. K. Cho, H. Moon and C. J. Kim, *Microelectromechanical Systems, Journal of*, 2003, **12**, 70-80.
12. L. H. Hung, K. M. Choi, W. Y. Tseng, Y. C. Tan, K. J. Shea and A. P. Lee, *Lab Chip*, 2006, **6**, 174-178.
13. X. Niu, S. Gulati and J. B. Edel, *Lab Chip*, 2008, **8**, 1837-1841.
14. D. Link, S. L. Anna, D. A. Weitz and H. Stone, *Physical review letters*, 2004, **92**, 54503.
15. W. Wang, C. Yang and C. M. Li, *Lab on a Chip*, 2009, **9**, 1504-1506.
16. T. Franke, A. R. Abate, D. A. Weitz and A. Wixforth, *Lab on a Chip*, 2009, **9**, 2625-2627.
17. L. Zhao, L. Pan, K. Zhang, S. Guo, W. Liu, Y. Wang, Y. Chen, X. Zhao and H. Chan, *Lab Chip*, 2009, **9**, 2981-2986.
18. N. T. Nguyen, T. H. Ting, Y. F. Yap, T. N. Wong, J. C. K. Chai, W. L. Ong, J. Zhou, S. H. Tan and L. Yobas, *Applied Physics Letters*, 2007, **91**, 084102-084102-084103.
19. S. H. Tan, S. Sohel Murshed, N. T. Nguyen, T. N. Wong and L. Yobas, *Journal of Physics D: Applied Physics*, 2008, **41**, 165501.
20. M. He, J. S. Edgar, G. D. M. Jeffries, R. M. Lorenz, J. P. Shelby and D. T. Chiu, *Analytical chemistry*, 2005, **77**, 1539-1544.
21. M. Ozkan, M. Wang, C. Ozkan, R. Flynn and S. Esener, *Biomedical Microdevices*, 2003, **5**, 61-67.
22. S. Zeng, B. Li, X. Su, J. Qin and B. Lin, *Lab on a Chip*, 2009, **9**, 1340-1343.
23. K. Ahn, C. Kerbage, T. P. Hunt, R. Westervelt, D. R. Link and D. Weitz, *Applied Physics Letters*, 2006, **88**, 024104.
24. J. C. Baret, O. J. Miller, V. Taly, M. Ryckelynck, A. El-Harrak, L. Frenz, C. Rick, M. L. Samuels, J. B. Hutchison and J. J. Agresti, *Lab Chip*, 2009, **9**, 1850-1858.
25. W. Wang, C. Yang, Y. S. Liu and C. M. Li, *Lab on a Chip*, 2010, **10**, 559-562.
26. M. Pollack, A. Shenderov and R. Fair, *Lab Chip*, 2002, **2**, 96-101.
27. A. R. Wheeler, *Science*, 2008, **322**, 539-540.
28. I. Barbulovic-Nad, H. Yang, P. S. Park and A. R. Wheeler, *Lab Chip*, 2008, **8**, 519-526.

29. K. Choi, M. Im, J. M. Choi and Y. K. Choi, *Microfluidics and Nanofluidics*, 2012, 1-7.
30. B. Ahn, K. Lee, R. Louge and K. W. Oh, *Biomicrofluidics*, 2009, **3**, 044102.
31. B. Ahn, K. Lee, R. Panchapakesan and K. W. Oh, *Biomicrofluidics*, 2011, **5**, 024113.
32. M. Hase, S. N. Watanabe and K. Yoshikawa, *Physical Review E*, 2006, **74**, 046301.
33. Y. M. Jung, H. C. Oh and I. S. Kang, *Journal of colloid and interface science*, 2008, **322**, 617-623.
34. X. Niu, M. Zhang, S. Peng, W. Wen and P. Sheng, *Biomicrofluidics*, 2007, **1**, 044101.
35. D. J. Im, J. Noh, D. Moon and I. S. Kang, *Analytical chemistry*, 2011.
36. D. R. Link, E. Grasland-Mongrain, A. Duri, F. Sarrazin, Z. Cheng, G. Cristobal, M. Marquez and D. A. Weitz, *Angewandte Chemie International Edition*, 2006, **45**, 2556-2560.
37. A. Carlson, M. Do-Quang and G. Amberg, *International Journal of Multiphase Flow*, 2010, **36**, 397-405.
38. L. Jiang, Y. Zeng, H. Zhou, J. Y. Qu and S. Yao, *Biomicrofluidics*, 2012, **6**, 012810.
39. M. Sussman, P. Smereka and S. Osher, *Journal of Computational Physics*, 1994, **114**, 146-159.
40. C. Elbuken, T. Glawdel, D. Chan and C. L. Ren, *Sensors and Actuators A: Physical*, 2011, **171**, 55-62.
41. M. Hashimoto, P. Garstecki, H. A. Stone and G. M. Whitesides, *Soft Matter*, 2008, **4**, 1403-1413.
42. F. Guo, X. H. Ji, K. Liu, R. X. He, L. B. Zhao, Z. X. Guo, W. Liu, S. S. Guo and X. Z. Zhao, *Applied Physics Letters*, 2010, **96**, 193701.
43. S.A.Vanapalli, A.G.Banpurkar, D.VanDenEnde, M. H. G. Duits and F. Mugele, *Lab Chip*, 2009, **9**, 982-990.